Ultramicroscopy 231 (2021) 113257

Contents lists available at ScienceDirect

Ultramicroscopy

journal homepage: www.elsevier.com/locate/ultramic

Efficient large field of view electron phase imaging using near-field electron ptychography with a diffuser

Frederick Allars [a,#], Peng-Han Lu [b,c,#], Maximilian Kruth [b,c], Rafal E. Dunin-Borkowski [b], John M. Rodenburg [a], Andrew M. Maiden [a,*]

[a] Department of Electronic and Electrical Engineering, Sir Frederick Mappin Building, University of Sheffield, S3 7HQ, United Kingdom
[b] Ernst Ruska-Centre for Microscopy and Spectroscopy with Electrons and Peter Grünberg Institute, Forschungszentrum Juelich, 52425 Juelich, Germany
[c] RWTH Aachen University, 52074 Aachen, Germany

ARTICLE INFO

Keywords:
Ptychography
Phase retrieval
Electron microscopy

ABSTRACT

Most implementations of ptychography on the electron microscope operate in scanning transmission (STEM) mode, where a small focussed probe beam is rapidly scanned across the sample. In this paper we introduce a different approach based on near-field ptychography, where the focussed beam is replaced by a wide-field, structured illumination, realised through a purpose-designed etched Silicon Nitride window. We show that fields of view as large as 100 μm^2 can be imaged using the new approach, and that quantitative electron phase images can be reconstructed from as few as nine near-field diffraction pattern measurements.

1. Introduction

Ptychography is a computational imaging technique first described in 1970 by Hoppe for electron microscopy [1], which has been developed into a popular form of coherent diffractive imaging in the last decade [2]. In ptychography, a sample is illuminated by a coherent, localised 'probe' beam of illumination. The sample diffracts the probe, generating an exit wavefront that propagates to form a diffraction pattern, whose intensity is recorded by a detector placed in the far-field. Either the sample or the probe is then translated laterally to change the region of the sample that the probe illuminates, making sure that this new region overlaps to some extent with the previous one. The detector records the intensity of the new diffraction pattern, then the process repeats until an area of interest on the sample has been illuminated by an overlapping patchwork of probe positions. Analytic [3,4] or iterative [5-8] inversion algorithms process the recorded diffraction intensities to reconstruct a complex-valued image of the sample that quantitatively maps out its transmission characteristics in both magnitude and phase. The illumination wavefront is usually recovered by these algorithms such that it has no influence on the sample image. The overlap between probe positions means ptychography is particularly robust and insensitive to noise, compared to other forms of coherent diffractive imaging, whilst the lateral translation at the heart of the technique naturally extends the field of view. These benefits, combined with ptychography's simple, single-optical path experimental process, have led to its wide adoption in both optical [9,10] and x-ray [11] microscopy. In electron microscopy, the advent of high speed direct-detection cameras has recently sparked great interest in applying the technique for ultra-high resolution imaging [12] as well as low dose imaging of biological samples [13].

Hoppe's original idea has inspired numerous variants, including near field ptychography, which was first realised in the x-ray domain [14]. Near-field ptychography replaces the localised probe illumination with full-field structured illumination and moves the detection plane from the far- to the near-field. The method has been relatively well-explored at X-ray wavelengths, where for example it has been combined with tomography for volumetric imaging [15] and requirements on the speckle size of the illumination have been characterized [16], whilst several versions of the method have also been implemented on light microscopy platforms [10,17]. These works have highlighted several advantages of the near-field approach to ptychography: a reduced requirement on the dynamic range of the detector, a larger field of view per diffraction pattern and a relaxation of the degree of coherence of the illumination [14,18]. In this paper, we demonstrate near-field ptychography on the transmission electron microscope (TEM) using a patterned silicon nitride membrane as a diffuser to randomly structure the electron beam.

* Corresponding author.
E-mail address: a.maiden@sheffield.ac.uk (A.M. Maiden).
# Both Authors contributed equally to this manuscript

https://doi.org/10.1016/j.ultramic.2021.113257
Received 28 September 2020; Received in revised form 10 February 2021; Accepted 27 February 2021
Available online 11 March 2021

Although adding additional components to the electron microscope to structure the illumination of the electron beam has some history, for example the implementation of electron phase plates [19], and there has been some early work on structured illumination for so-called "4D STEM" electron ptychography [20,21], structured illumination, near-field electron ptychography is new. Earlier work on near-field electron ptychography did not use a diffuser but just a standard aperture [22]. This limited the system to a small field of view per diffraction pattern, so, like conventional far-field electron ptychography, covering a reasonable field of view required hundreds (or thousands) of scan points. Use of a diffuser here allows us to maximise the use of the detector bandwidth to capture a large field of view for every diffraction pattern in the ptychographic data set. Instead of hundreds of diffraction patterns, we show that as few as nine diffraction patterns are sufficient to recover a high quality, quantitative, large field of view phase image. Additionally, using a reasonable number of diffraction measurements we show that field of view can be extended to 100 μm^2 at a resolution of better than 4 nm.

2. An implementation of near-field ptychography in the TEM

The microscope configuration we use mirrors previous visible-light microscope adaptations [17] and is shown in Fig. 1a. The sample is illuminated by a broad, roughly parallel electron beam (convergence angle ~0.5mrad). The objective lens forms an image of the sample in the plane of the selected area aperture strip. A 50 μm-diameter Si_3N_4 diffuser inserted in the aperture strip (see Methods section) modulates the image wavefront, which travels on through the microscope projector and diffraction lenses to a scintillator and CCD detector. The diffraction lens is operated at a defocus such that the CCD records the wavefront as it would be in a plane 77 cm further down the column. An exemplar diffraction pattern from the setup is shown in Fig. 1b. These recordings are near-field diffraction patterns, with an effective Fresnel number of 412 (a Fresnel number >> 1 corresponds to near-field diffraction. For comparison, earlier work [22] on near-field electron ptychography operated with a Fresnel number of 17.2). To gather data for ptychographic reconstruction the microscope's motorised translational stage moves the sample through a grid of positions and the resulting set of near-field diffraction patterns are recorded, all under the control of custom digital micrograph (DM) scripts. The dimensions and step size of the position grid determine the field of view of the eventual sample image.

Our configuration can be thought of as equivalent to conventional near-field ptychography if one imagines a virtual diffuser shrank down by a factor equal to the magnification of the objective lens and positioned just upstream of the sample so that it structures the incident electron beam. The objective lens of the microscope used in our experiments operates at a magnification of 59 times, so the diffuser projected back through the lens gives a virtual structured illumination on the sample with a diameter of 850 nm. The sample effectively translates

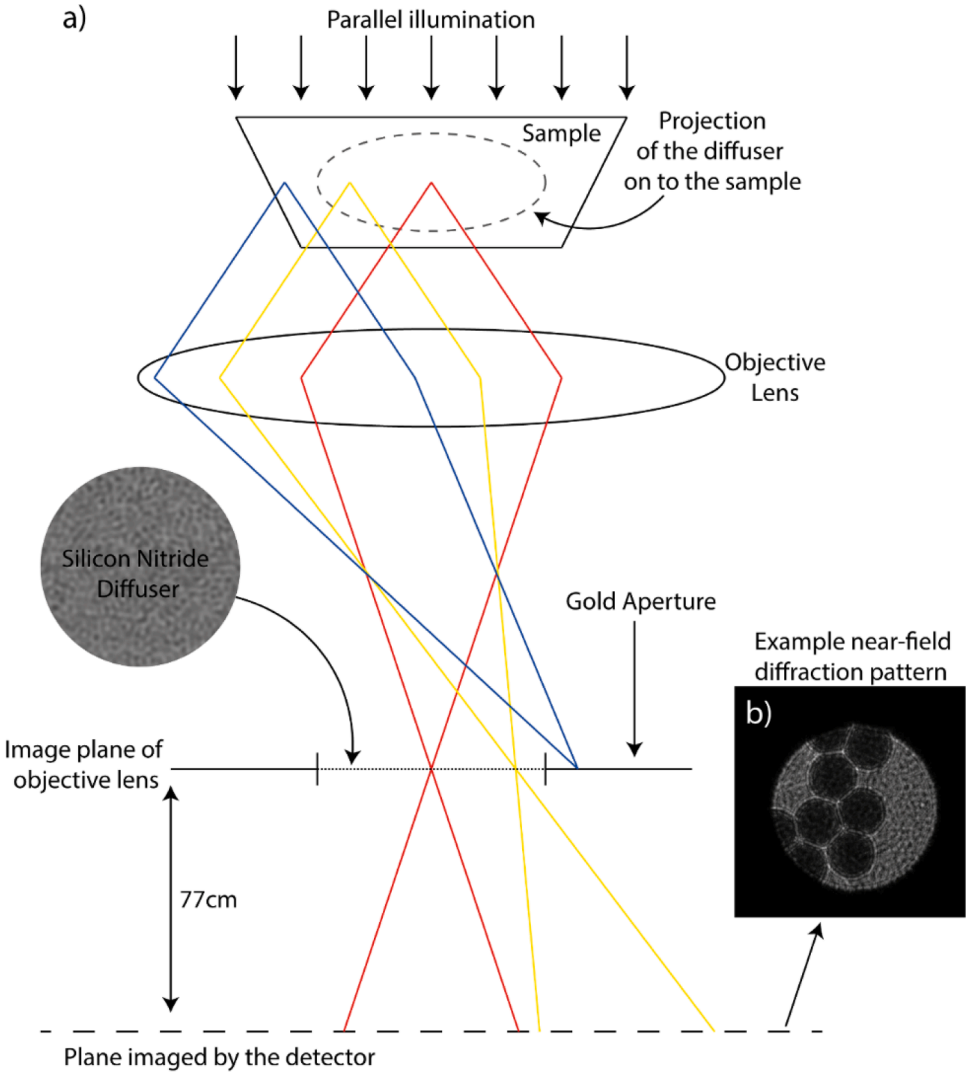

Fig. 1. a) Microscope setup. The image formed by the microscope objective lens is modulated by a Silicon Nitride diffuser located in the selected area aperture strip. The microscope is operated in diffraction mode with a large defocus on the diffraction lens, such that the detector records near-field diffraction patterns at an effective distance of 77 cm from the selected area plane. The sample is translated through a grid of positions such that the image formed by the objective lens translates across the diffuser in small steps, realising the required ptychographic overlap. b) An example near-field diffraction pattern recorded from the setup, showing latex spheres in the field of view (darker circles) and the modulation of the diffuser (the background speckle).

through this virtual illumination, over a grid of positions with a spacing around 10–20% of its diameter to ensure overlap between the illuminated sample areas. The defocus introduced by the diffraction lens equates to an imaging plane 221 μm downstream of the sample in this 'virtual' setup.

There are alternative ways to configure a TEM for near-field ptychography. For example, the diffuser could be mounted in the condenser aperture to structure the illumination and the beam could be scanned rather than translating the sample. Our particular method has advantages and disadvantages. On the plus side, the phase image of the sample in the selected area plane is reconstucted in this configuration (as in off-axis holography), so imaging thicker samples is possible, whereas thick samples in a more conventional pre-sample illumination scheme result in breakdown of the multiplicative sample-beam interaction upon which ptychographic algorithms rely. Alignment and calibration in our configuration is straightforward, simply following a standard brightfield TEM process. Translating the sample avoids any changes to the microscope optics during the experiment. On the negative side, positioning the diffuser aperture after the sample cuts out valuable counts making our configuration less dose efficient, and the sample translation (at least here without a piezo stage) is quite slow.

3. Experimental results

We implemented the configuration shown in Fig. 1a on an FEI Titan 80–300 STEM at the Ernst-Ruska Centre in Juelich, Germany. Although the microscope is a probe-corrected STEM instrument, it was operated as an uncorrected TEM for these experiments. Preliminary testing of data collection code and optimisation of lens settings were carried out on the JEOL R005 microscope at the University of Sheffield [23].

Several experimental parameters were varied to evaluate their effect on the image reconstruction. The parameters investigated were the minimum number of diffraction patterns, the effect of energy filtering, low spatial frequency phase recovery, the extension to extremely large fields of view and the influence of the diffuser phase profile on the image quality. The collected data were processed and images reconstructed by a modified form of the 'ePIE' iterative ptychographic algorithm [22], which also recovered the diffuser transmission characteristics so it did not need to be characterised ahead of time. Throughout, our sample was a 463 nm-periodicity diffraction grating replica, populated with 262 nm-diameter latex spheres whose known shape allowed us to assess the accuracy of the phase reconstructions (Ted Pella Product No. 603).

3.1. Minimum number of diffraction patterns

Our first experiments investigated the minimum number of diffraction patterns required to provide sufficient data to reconstruct quantitative, low noise electron phase images, mirroring studies in the X-ray and visible light imaging modalities [16,17]. For these tests we used a Gatan Imaging Filter (Tridiem 866 ERS) to select the zero-loss peak (slit width of 20 eV) and thereby remove a portion of the inelastic scattering background from the recorded data. The scan step size was 100 nm (12% of the virtual diffuser diameter) and the scan grid size ranged from 2 × 2 to 5 × 5 positions. The results of these experiment are shown in Fig. 2. The images for the 5 × 5 and 4 × 4 grid sizes give closely matched image quality with little noise visible. For the 3 × 3 grid, we required a reasonably good initial estimate of the diffuser phase profile (taken from the 5 × 5 scan grid data) to seed the reconstruction, but the eventual image quality remains high (note, though, the slightly reduced field of view as the number of diffraction patterns reduces). Quality drops off significantly for the 2 × 2 scan grid, although there is still some structure identifiable in the phase image. This is expected: with only four diffraction patterns there is insufficient information contained in the recorded data to condition the reconstruction process, i.e. there are less measured data points than there are reconstructed pixels. These results tie in with the work of Clare and colleagues who showed a good X-ray

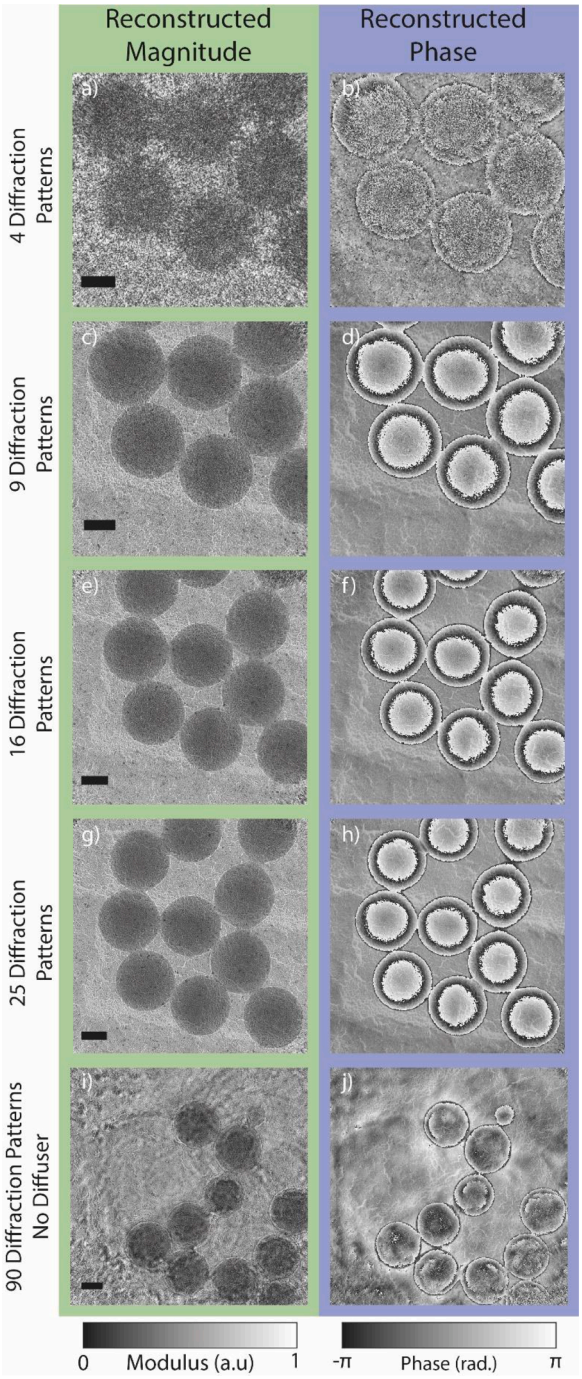

Fig. 2. Reconstruction quality as a function of the number of diffraction patterns recorded. a), c), e), g) show the reconstructed magnitudes and b), d), f), h) the reconstructed phases from ptychographic scans over square grids of sizes 2 × 2, 3 × 3, 4 × 4, and 5 × 5, each with a 100 nm scan step size. Note the field of view expands as the number of diffraction patterns increases. i) and j) show the reconstructed magnitude and phase when the diffuser was not present in the experiment. Scale bars 100 nm.

image reconstruction from near-field ptychography using 16 diffraction patterns [17]. To show the efficacy of the diffuser in modulating the diffraction data, we also carried out an identical experiment using a standard selected area aperture, without the diffuser. The results in Figs. 2i and 2j, although surprisingly not completely illegible, demonstrate that diffraction from the edges of the aperture provide insufficient diversity in the diffraction data to allow quantitative phase imaging.

The latex spheres provide a means to quantitatively assess the phase

accuracy of the images in Fig. 2. Since the diameter of the spheres can be measured from the reconstructed images, their thickness is easily determined by assuming an ideal spherical shape. By equating this thickness to the unwrapped reconstructed phase profile, the mean inner potential of the latex can be ascertained [22]. For the 3 × 3 reconstruction, the mean inner potential was calculated as 8.43 V, with a standard deviation of 0.39 V across the 8 spheres as labelled in the unwrapped phase image of Fig. 3. This aligns well with previous measurements [22,24] of 7.9 V (std 0.64 V) and 8.4 V (std 0.7 V). The measured mean inner potential for the 16 diffraction pattern reconstruction was 8.45 V with a standard deviation of 0.44 V and it was 8.54 V with a standard deviation of 0.35 V for the 25 diffraction patterns case. Plots of the radial average unwrapped phase of the 8 spheres from the 25 diffraction pattern reconstruction, shown in Fig. 3b, exhibit good correlation to the ideal spherical shape.

3.2. The effect of energy filtering

The inherent redundancy of ptychographic data, introduced by the overlap between illuminated areas of the sample at each sample position, means that ptychographic reconstruction algorithms can compensate for many additional sources of noise, including partial beam coherence, low counting statistics and sample positioning inaccuracies. For TEM-based ptychography, one such noise source is the incoherent background signal caused by inelastic scattering from the sample, and in our case also from the Si_3N_4 diffuser. Our ptychographic algorithm attempts to separate the additional background of the diffuser from the coherent elastic signal. To test its effectiveness we carried out a second experiment, collecting two data sets, one with zero-loss energy filtering (20 eV slit width) and the other without any filtering. Experimental parameters were as for the minimum scan size experiments, except for an increased 10×10 grid size. Direct Comparison of the energy filtered and non-energy filtered reconstructions was not possible as the latex spheres shrank slightly between experiments, so instead each data set was split in two by separating odd and even diffraction patterns (thereby increasing the step size). This allowed us to carry out two independent reconstructions from each data set to provide two independent images of the sample for comparison via Fourier ring correlation (FRC) [25-27]. This process is similar to one method of assessing the frequency response of inline holography: a series of defocused images are split into two data sets which are reconstructed independently and compared via FRC [28]. The FRC was calculated from the 800 by 800 pixel central region of the two separate reconstructions. Prior to the FRC these regions were registered to sub-pixel accuracy and they were normalised to the same mean phase.

The results are shown in Fig. 4. Both the energy filtered and non-energy filtered results give values for the mean inner potential of the latex spheres within one standard deviation of previous results. The mean inner potential for the energy filtered reconstruction is 8.47 V with a standard deviation of 0.43 V and for non-energy filtered case the mean

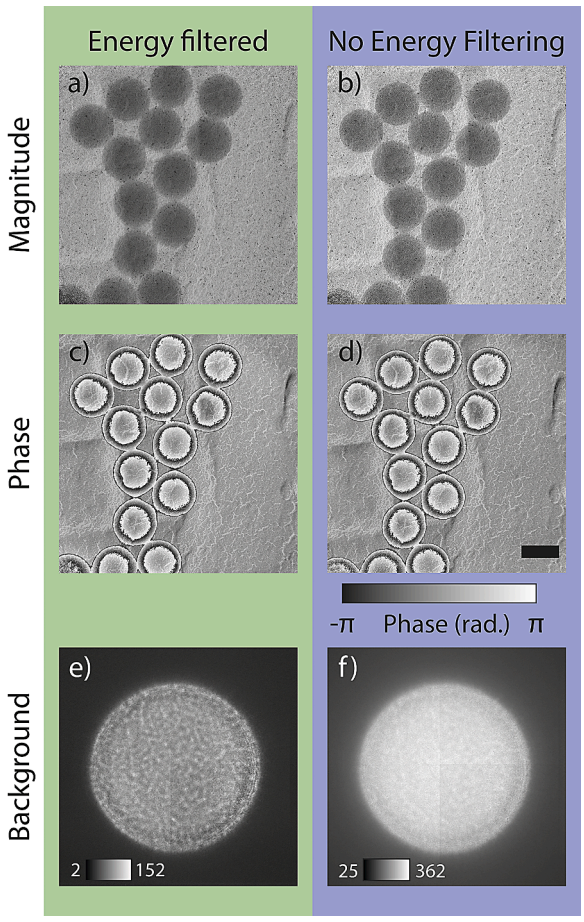

Fig. 4. a) and c) are the reconstructed magnitude and phase from an energy-filtered data set with a 20 eV energy slit. b) and d) are reconstructed magnitude and phase from a non-energy-filtered data set. Scale bar in d) is 200 nm and applies to a)-c). Grey scale colour bar corresponds to the phase shift in radians. e) and f) represent the background modelled by the reconstruction algorithm for the energy filtered and non-energy filtered data sets, respectively. The colour bar insets in e) and f) show their minimum and maximum intensity values.

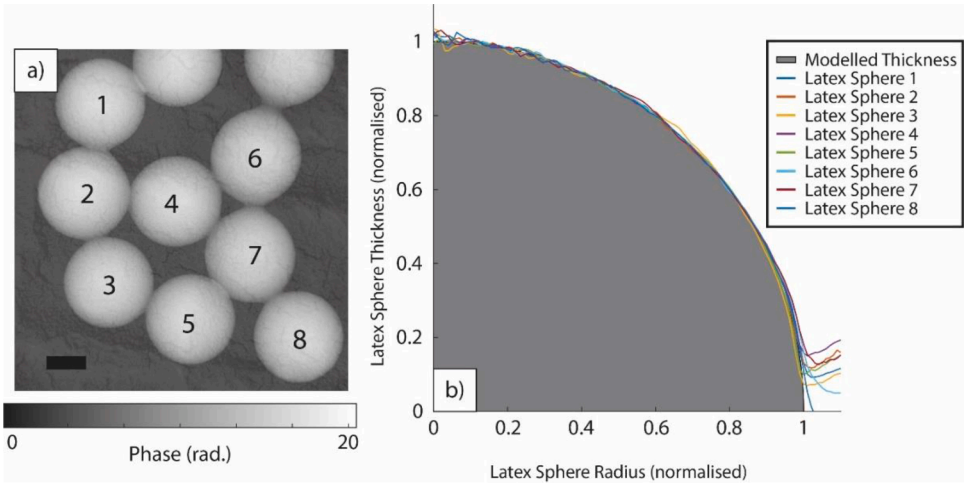

Fig. 3. The unwrapped phase of Fig. 2h with latex spheres numbered. The mean inner potential of the latex was measured for each of these spheres and the results averaged to give the statistics listed in the main text. The scale bar is 100 nm. In b) the grey area demarks a perfect spherical profile, whilst the plots are the radially averaged phase of the latex spheres numbered in Fig. 3a). The plots are scaled to take account of the differing diameters of the latex spheres, and hence are shown on unitless axes.

inner potential is 8.67 V with a standard deviation of 0.45 V. The reconstruction algorithm extracts a background signal from the data which is assumed to be constant in every diffraction pattern, in order to mitigate for inelastic scatter from the diffuser and any average background inelastic scatter from the sample. These backgrounds are shown in Figs. 4e and 4f for the energy filtered and unfiltered data sets, showing a significant increase in inelastic background when the filter is not used. The sharp lines segmenting the image into four quadrants correspond to different readout zones of the CCD camera. The slightly darker rings near the edges of the disc in these backgrounds correspond with strong fringes in the diffraction data caused by the edge of the diffuser aperture. That these fringes affect the background signal indicates some cross-talk between the background extraction and the probe/diffuser reconstruction, which we are currently investigating.

Fig. 5. shows the results of the Fourier ring correlation of the energy filtered and non-energy filtered data sets. The half-bit threshold was used as a resolution measure [25]. The non-energy filtered FRC intersects it at a frequency of 0.268 nm^{-1} and the energy filtered FRC intersect it at frequency of 0.298 nm^{-1}, corresponding to real-space resolutions of 3.73 nm for the non-energy filtered reconstructions and 3.36 nm for the energy filtered case.

3.3. Low spatial frequency recovery

Fig. 5 demonstrates strong correlation between independent phase images across a wide range of spatial frequencies. That the lowest spatial frequencies correlate well could be explained by the initial conditions of the two reconstruction processes, which were both initialised with a flat phase. To remove this potential bias, the two energy-filtered data sets were reconstructed again, this time with the strong, random low spatial frequency initial phase profiles shown in Figs. 6a and 6b. The reconstructed phase images in Figs. 6c-d demonstrate robust recovery from these random initialisations, apart from close to the edges of the reconstruction area. Phase recovery in these peripheral regions is less well conditioned because they contribute to relatively few of the recorded diffraction data. Comparison of the reconstructions via FRC

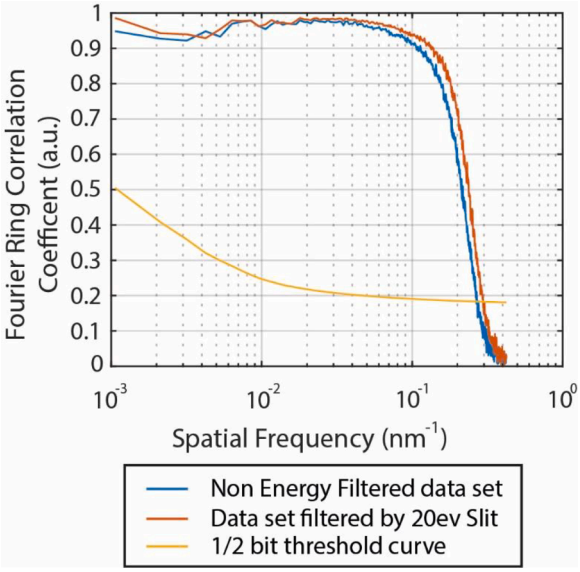

Fig. 5. Fourier Ring Correlation analysis of two independent reconstructions of the same sample area from energy filtered diffraction data, and two independent reconstructions from non-energy filtered data. A 1/2-bit threshold curve is included as reference to display the difference in signal to noise ratios between the two correlations. The intersection of this curve with the correlation curves gives an indication of resolution in the reconstruction: for the reconstruction using unfiltered data this calculation gives a resolution of 3.73 nm and for the filtered data the resolution is estimated at 3.36 nm.

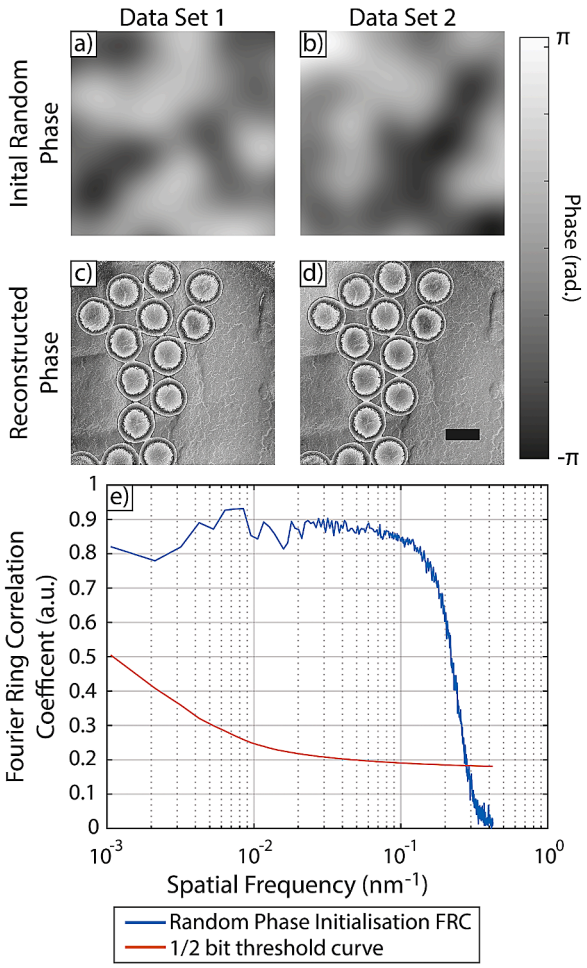

Fig. 6. An assessment of low spatial frequency sensitivity. Two sets of diffraction patterns from the same sample area were reconstructed independently. The two reconstruction processes were seeded with the random low spatial frequency phase profiles shown in a) and b). The respective recovered phase images are shown in c) and d). The central parts of the phase images (corresponding to the region fully covered by the different sample positions) were extracted and compared via FRC as shown in e). The Scale bar in d) is 200nm and applies to a) - c).

proceeded as in Section 3.2, except that in this case a relative linear ramp between the two phase images was removed. This is a known ambiguity in ptychography [5]. Although it still shows good correlation at low spatial frequencies, the FRC plot in Fig. 6e dips slightly across the full range of spatial frequencies, relative to Fig. 5, which we attribute to errors at the edges of the reconstruction. The intersection with the 1/2bit threshold is unaffected. Optimising the experimental setup to better recover low spatial frequencies is an interesting area for further exploration, for example by changing the camera length or increasing the spatial frequency bandwidth of the diffuser design. Algorithms adapted from inline holography may also assist in low spatial frequency recovery [28,29].

3.4. Extremely large field of view

The objective of our next experiment was to demonstrate electron phase imaging over a field of view that is difficult to obtain using other methods. The experiment also investigated the stability of the data collection over longer experimental times and with larger step sizes. To maximise field of view, we used a step size of 250 nm and scanned over a 40×40 position grid. The diffraction patterns collected in this data set were not energy filtered.

Fig. 7. displays the amplitude and phase of the reconstructed sample image. The field of view is close to 100 μm^2 and the image contains 65 megapixels. Put another way, each diffraction pattern adds 0.0625 μm^2 and 40,600 pixels to the image. This compares favourably with earlier work [22] where each diffraction pattern contributed 0.005 μm^2 and 1400 pixels. It is interesting to observe in the phase image a dark halo around the isolated latex spheres, but not around the large cluster of spheres in the bottom left corner. We speculate that this additional phase contrast (dark halo) is due to electron beam-induced charging of these dielectric spheres, while the agglomerated latex cluster may be less sensitive to charging, possibly because of the different surface structure. This could be tested by coating the sample in a thin layer of amorphous carbon to prevent the accumulation of surface charge without significantly changing the mean inner potential of the specimen. The average of the MIP values of the cluster of latex spheres in the bottom left of the field of view is 8.64 V with a standard deviation of 0.85 V. Image quality in this reconstruction is consistent across the entire image but visibly lower than previous results, which we attribute to a much larger step size.

Over the course of data collection for the images in Fig. 7, the microscope optical axis drifted markedly and required an additional algorithmic step to correct (this step and a complete run through of the reconstruction algorithm can be found in the supplement to reference 22). Additionally, the step size in this experiment, equating to 30% of the diffuser diameter, was large by the standards of ptychography. Combined, the drift and large step size may be the cause of the 'cloudy' low spatial frequency background in Fig. 6b. To give an idea of low spatial frequency robustness, even under these less than ideal experimental conditions, we ran a second reconstruction from the large field of view data using the strong low frequency phase initialisation shown in Fig. 8a. The resulting phase image in Fig. 8b, although distorted by a very low frequency background, has clearly recovered remarkably well from the random initial conditions, and the dark halos surrounding the isolated latex spheres are again evident in the image. The disc in the top right corner of Fig. 8b indicates the dimensions of the diffuser aperture, relative to the sample, and it is interesting to note that features in the low frequency background are of approximately this dimension; perhaps unsurprising given the movement of the optical axis between each scan point in the experiment.

3.5. Comparison of performance using different diffusers

One of the advantages of ptychography is that, apart from reconstructing the sample image, ptychographic algorithms also recover the transmission characteristics of the illumination, i.e. the diffuser in our case, so it need not be characterised separately. We tested several diffuser designs during the course of our experiments and Fig. 9. shows the reconstructed magnitude and phase profiles of four of them, all reconstructed from ptychographic data captured using a 100 nm step size and a 10 × 10 scan pattern. The strong correlation between the phase images in the second and third column indicates that the pre-calibrated FIB-milled depth profiles resulted in real-world phase shifts very close to their designed value. To quantify this, looking at diffuser 4, the designed phase shift of the squares in the diffuser (Fig. 9l) with respect to the background was 2.35 radians for 300 *k*eV electrons. The average phase of these squares in the reconstruction shown in Fig. 9k is

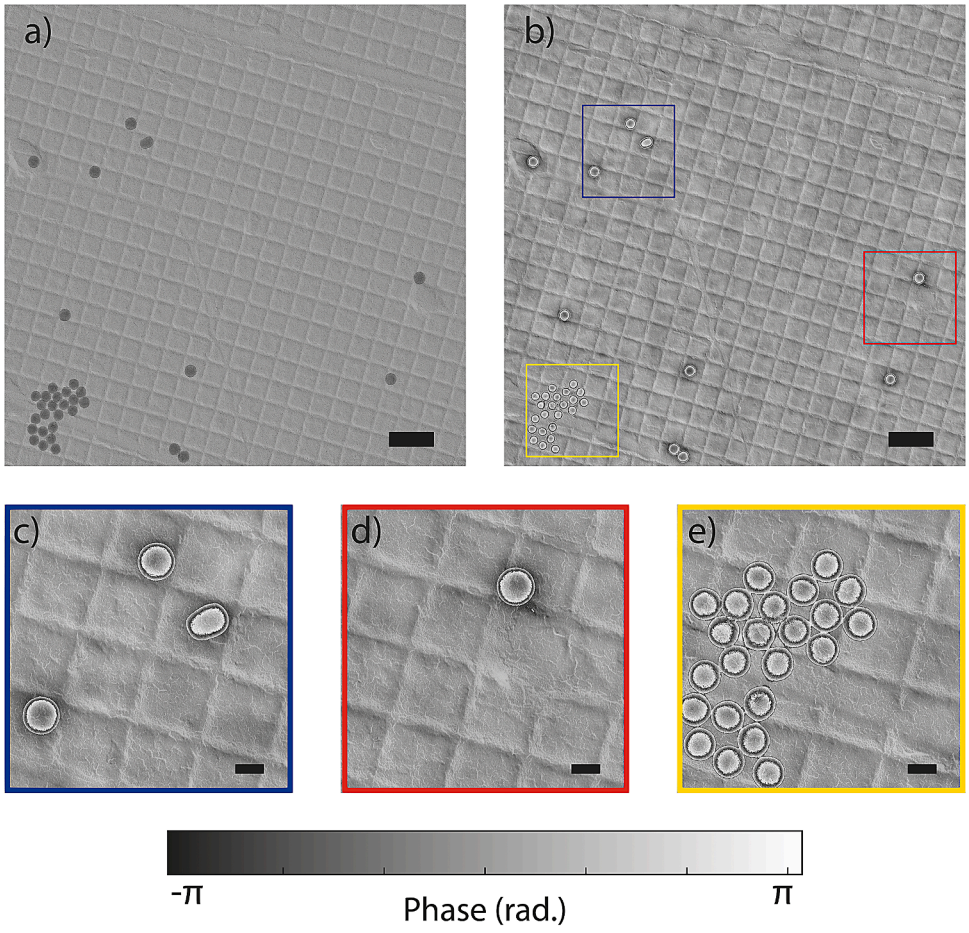

Fig. 7. a) Magnitude and b) phase images of a 100 μm^2 sample area, reconstructed from 1600 diffraction patterns. c)-e) show enlarged subsections of b), each corresponding to the boxes in b) with the same colour. Note the halos around the latex spheres in c) and d), which are not present around the cluster of spheres in e). Note also the melted sphere in c). Scale bars in a) and b), 1 μm. Scale bars in c)-e), 200 nm.

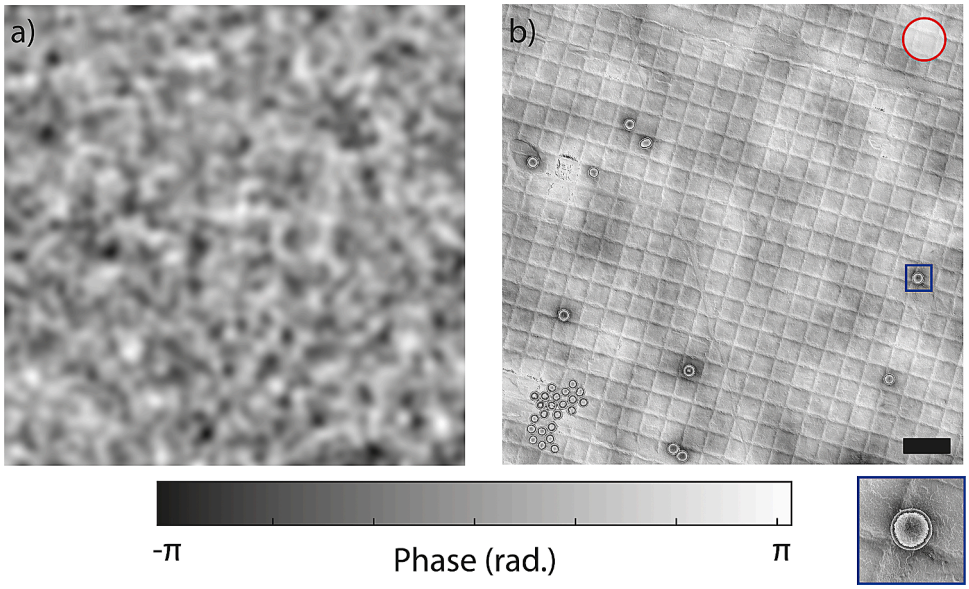

Fig. 8. Large field of view phase reconstruction, with a random phase initialisation. a) shows the initial object phase fed to the reconstruction algorithm, b) shows the final phase image. The circle in the top right indicates the size of the diffuser aperture. The zoom shows the dim phase 'halo' still surrounding the boxed latex particle. Scale bar, 1 μm.

2.18 radians with a standard deviation of 0.07 radians.

Unexpectedly, the reconstructed phase of the diffusers often features strong, low-frequency phase gradients, e.g. at the bottom right-hand corner of Fig. 9h. These are unlikely to be a reconstruction artefact, since they appear consistently for a given diffuser over completely separate experiments, and regardless of the initial 'seed' diffuser profile fed to the reconstruction algorithm. There are two further possible explanations. One is charging of the insulating thin film diffuser or its diaphragm [30], the other is optical aberrations from condenser or diffraction lenses. The former issue is more likely to be the problem. However, it is still comforting that such an artefact in the "illumination" does not degrade the phase imaging results of the sample of interest.

4. Discussion

In further developing near-field electron ptychography, our primary objective is to improve the data collection process. Currently, we are able to collect a diffraction pattern every 3 s, comprising 0.5 second for CCD exposure and 2.5 s for image readout, saving the image, stage movement and stage settling. This translates into data collection times for the 25, 16, 9, and 4 diffraction pattern data sets in Section 3.1 of 77 s, 48 s, 29 s and 11 s respectively. The large field of view data set took 88 min to collect. We are working on improving data collection through an automated workflow, a faster camera and an efficient scanning approach, such as using the image beam shift, a piezo-driven stage, or hybrid beam shift-stage scanning [31].

A second objective is to push the resolution and investigate the frequency response of the method. The resolution obtained in the work reported here – around 3.4 nm – is limited by the detector pixel size and the magnification of the projector lens system. Whilst we envisage near-field ptychography primarily as a tool for wide field of view phase imaging rather than imaging at the atomic level, the ultimate achievable resolution should be governed by the information limit of the TEM objective lens. Performance and resolution will also be affected by beam coherence (and therefore the effective electron source size [32]), noise in the recorded data, and the spatial frequency content of the diffuser design. The FRC comparison in Section 3.2 shows good low spatial frequency correlation between image reconstructions, but this requires verification for very large fields of view and for less structured samples (for example free space electric fields).

The use of a diffuser in electron ptychography holds particular promise for low-dose phase imaging [20], so a third objective is to investigate and reduce dose requirements for beam sensitive samples. To reduce the dose we can take advantage of beam blanking between exposures, and we can reposition the diffuser in the condenser aperture strip to ensure all parts of the sample exposed to the beam contribute directly to the recorded data. We can also replace the diffuser with an electrostatic phase plate [33,34] to reduce inelastic background and maximise the useful counts on the detector.

A comparison with alternative phase imaging methods – in-line and off-axis holography, differential phase contrast, as well as far-field ptychography – awaits us once our experimental process is optimised. In particular we intend to compare the performance of near-field ptychography to the latest implementations of off-axis holography and through-focal series reconstruction [28], in order to ascertain whether near-field ptychography provides a better low frequency response over large fields of view. This benefit would be particularly appealing for imaging long-range electric fields in free-space, which may extend over many tens or hundreds of microns. Applying an unperturbed reference wave for off-axis holography is problematic in this application, and there is very little image variation with defocus for in-line holography.

5. Conclusion

This paper demonstrates a novel form of near-field ptychography in the TEM that employs a structured diffuser located in the microscope selected area aperture strip. We have shown how the technique can be used to efficiently realise accurate, large field of view electron phase imaging, from as few as nine diffraction patterns. The inherent diversity and redundancy in ptychographic data allowed us to solve for the transmission characteristics of the diffuser, which therefore did not need to be known a priori, as well as to compensate for inelastic scattering without zero-loss energy filtering. Quantitative analysis of our results show competitive phase accuracy, good low frequency response, and a resolution of around 3.4 nm.

There are many potential experimental configurations for ptychography in the TEM and STEM, and the efficacy with which ptychographic algorithms can handle shortcomings in the data holds great promise for the future of this research field. For example, this initial work on the use of a diffuser can expand in many directions, from low-dose phase

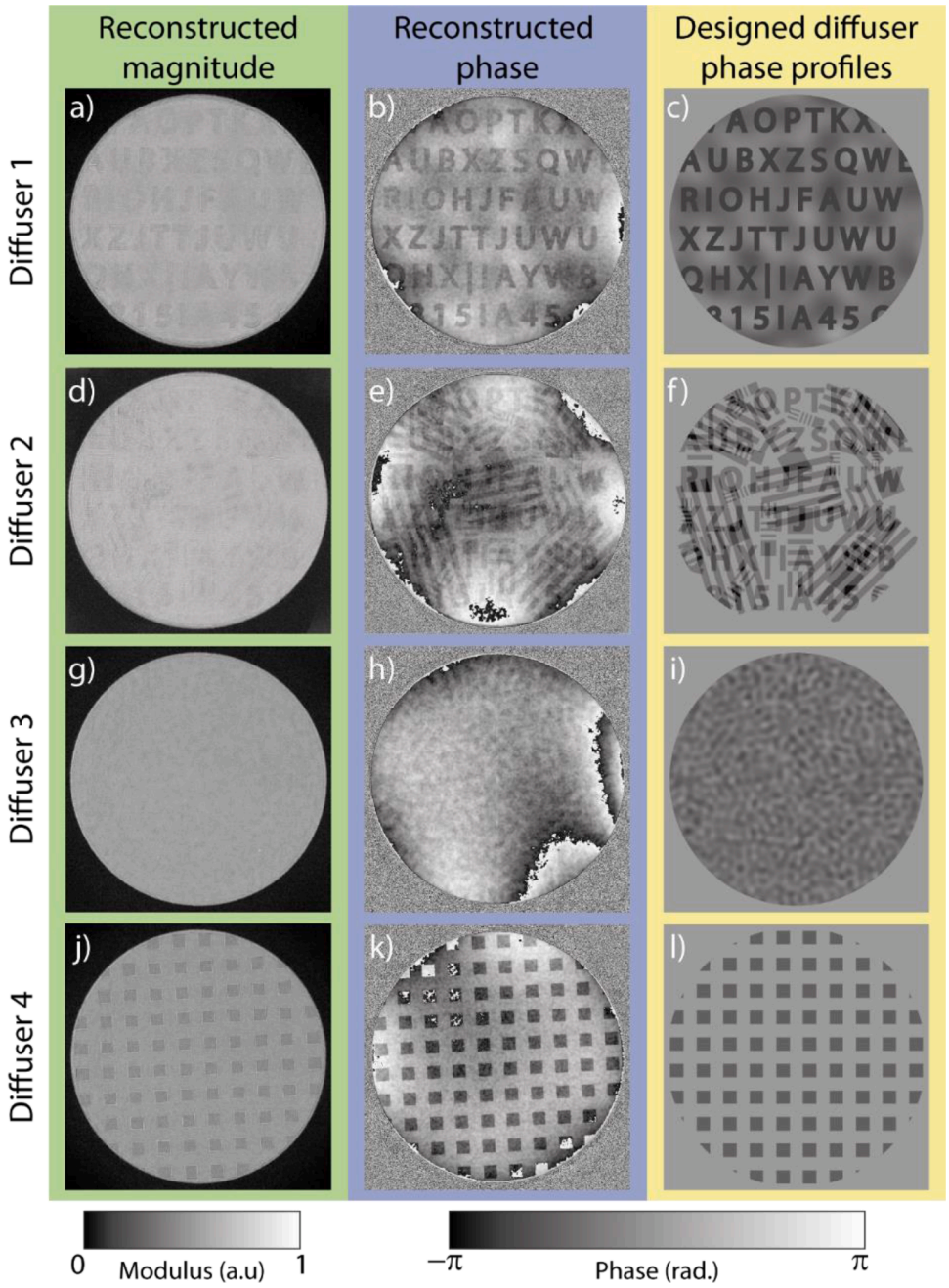

Fig. 9. Several different diffuser designs were trialled during our experiments, and in each case the ePIE algorithm recovered their transmission profiles along with the reconstructed sample image. The match between these reconstructions and the designed diffuser phase gives another indication of the accuracy of our images. a), d), g) and j), reconstructed magnitude of various diffusers, b), e), h) and k), reconstructed phase of various diffusers, and c), f), i) and l), designed phase of the corresponding diffusers. The diffusers are all 50 μm in diameter.

imaging to electron phase tomography. By drawing on the experience of those working on ptychography in optical and x-ray microscopy, electron ptychography can quickly advance toward real-world application and wide-spread use.

6. Methods

The data used in this investigation was collected by FEI Titan 80–300 STEM operating in an uncorrected TEM diffraction mode. The acceleration voltage of the electron gun was 300 keV and the spot size number was 3. The beam convergence semi-angle was approximately 0.5mrad. The objective lens magnification was calibrated at 59 times. Energy filtered data sets were filtered via a Gatan Imaging Filter (Tridiem 866 ERS) using a 20 eV energy slit. The camera used was a Gatan UltraScan CCD with 2048 × 2048 pixels and a 14 μm pixel size. The data was binned by 2 and exposures were all 0.5 s.

The diffraction lens strength was adjusted in order to convert the diffraction pattern typically seen in the TEM diffraction mode to a defocused image of the sample with the diffuser (see Fig. 1b). In this diffraction condition the combined magnification of the post-diffuser lens system was measured (using the known diameter of the diffuser window as a reference) as 402x. The defocus of the diffraction lens, measured with respect to the diffuser plane, was found by recording the diffraction pattern from a standard 50 μm selected area aperture and comparing this measurement with simulation. This gave a defocus of 77 cm, equating to an effective defocus relative to the specimen plane of 221 μm.

The diffusers were manufactured using focused ion beam milling, with spatially patterned etched depth difference producing designed phase shifts within the range 0–2.35 radians (for 300 *k*eV electrons). The thickness-modulated phase shift was pre-calibrated as a function of ion beam current and dwell time. The surround of the 50 μm-diameter

diffusers were covered by a ~150 nm-thick gold layer as a diaphragm and a charging alleviation layer.

The specimen was translated using the FEI CompuStage motorised positioning stage programmed through custom digital micrograph (DM) scripts, which also synchronised the camera exposures. To reduce backlash from the positioning stage (which had no piezo-drive function), at the end of each row of positions the stage return was over-scanned by 500 nm, before being brought back to the beginning of the next row. Since the movement of the sample across the diffuser aperture was visible in the recorded near-field data, we were also able to determine the actual grid of sample positions by cross-correlation of the data. From this we verified that the stage readout of sample positions was reasonably accurate and highly repeatable for the range of grid and step sizes we used.

Full details of the modified reconstruction ePIE algorithm can be found in the supplement of reference 21 and the Matlab code for the algorithm (along with example data sets) is available upon request from the authors. As well as recovering the sample image, the algorithm also solves for the diffuser transmission characteristics, models partial coherence, removes an inelastic background from the data, corrects small stage positioning errors, and compensates for any optical axis drift in the data.

Declaration of Competing Interest

The authors declare that they have no known competing financial interests or personal relationships that could have appeared to influence the work reported in this paper.

Acknowledgements

The research leading to these results has received funding from the European Union's Horizon 2020 research and innovation programme under grant agreement No. 823717 (ESTEEM 3) and No. 766970 (Q-SORT), as well as from a Royal Society International Exchange Award No. IESR2192202. F.A. is funded through the Engineering and Physical Sciences Research Council (EPSRC) Doctoral Training Partnership. The authors are grateful to the fruitful discussions with Prof. Giulio Pozzi (University of Bologna) on the electron beam induced charging of latex particles. We would like to acknowledge the help of Colm O'Regan from the Sorby Centre for Electron Microscopy, University of Sheffield, for the initial planning and set up of the experiments.

References

[1] R. Hegerl, W. Hoppe, Dynamic theory of crystalline structure analysis by electron diffraction in inhomogeneous primary wave field, Berichte Der Bunsen-Gesellschaft Fur. Physikalische Chemie. 74 (1970) 1148.
[2] Rodenburg, J. & Maiden, A. in *Springer Handbook of Microscopy* (eds Peter W. Hawkes & John C. H. Spence) 2-2 (Springer International Publishing, 2019).
[3] J.M. Rodenburg, R.H.T Bates, The theory of super-resolution electron microscopy via Wigner-distribution deconvolution, Philos. Trans. Royal Soc. London. Series A: Phys. Eng. Sci. 339 (1992) 521–553.
[4] H. Yang, et al., Simultaneous atomic-resolution electron ptychography and Z-contrast imaging of light and heavy elements in complex nanostructures, Nat Commun 7 (2016) 12532.
[5] A. Maiden, D. Johnson, P. Li, Further improvements to the ptychographical iterative engine, Optica 4 (2017) 736–745.
[6] M. Odstrčil, A. Menzel, M. Guizar-Sicairos, Iterative least-squares solver for generalized maximum-likelihood ptychography, Opt Express 26 (2018) 3108–3123.
[7] P. Thibault, A. Menzel, Reconstructing state mixtures from diffraction measurements, Nature 494 (2013) 68–71.
[8] P. Thibault, M. Guizar-Sicairos, Maximum-likelihood refinement for coherent diffractive imaging, New J Phys 14 (2012), 063004.
[9] J. Marrison, L. Raty, P. Marriott, P. O'Toole, Ptychography - a label free, high-contrast imaging technique for live cells using quantitative phase information, Sci. Rep. 3 (2013).
[10] H. Zhang, et al., Near-field Fourier ptychography: super-resolution phase retrieval via speckle illumination, Opt Express 27 (2019) 7498–7512.
[11] F Pfeiffer, X-ray ptychography, Nat Photonics 12 (2018) 9.
[12] Y. Jiang, et al., Electron ptychography of 2D materials to deep sub-ångström resolution, Nature 559 (2018) 343–349.
[13] L. Zhou, et al., Low-dose phase retrieval of biological specimens using cryo-electron ptychography, Nat Commun 11 (2020) 2773.
[14] M. Stockmar, et al., Near-field ptychography: phase retrieval for inline holography using a structured illumination, Sci. Rep. 3 (2013).
[15] M. Stockmar, et al., X-ray nanotomography using near-field ptychography, Opt Express 23 (2015) 12720–12731.
[16] R.M. Clare, M. Stockmar, M. Dierolf, I. Zanette, F. Pfeiffer, Characterization of near-field ptychography, Opt Express 23 (2015) 19728–19742.
[17] S. McDermott, A. Maiden, Near-field ptychographic microscope for quantitative phase imaging, Opt Express 26 (2018) 25471–25480.
[18] J. Hagemann, T. Salditt, Coherence-resolution relationship in holographic and coherent diffractive imaging, Opt Express 26 (2018) 242–253.
[19] R. Danev, K. Nagayama, Transmission electron microscopy with zernike phase plate, Ultramicroscopy 88 (2001) 243–252.
[20] P.M. Pelz, W.X. Qiu, R. Bücker, G. Kassier, R.J.D Miller, Low-dose cryo electron ptychography via non-convex bayesian optimization, Sci Rep 7 (2017) 1–13.
[21] W. Van den Broek, et al., Towards ptychography with structured illumination, and a derivative-based reconstruction algorithm, Microsc. Microanal. 25 (2019) 58–59.
[22] A.M. Maiden, M.C. Sarahan, M.D. Stagg, S.M. Schramm, M.J. Humphry, Quantitative electron phase imaging with high sensitivity and an unlimited field of view, Sci Rep 5 (2015) 14690.
[23] I.M. Ross, M. Kawazu, H. Sawada, A. Papworth, T. Walther, Performance of a cold-field emission gun double aberration corrected TEM/STEM at 80 kV, J. Phys.: Conference Series 371 (2012), 012013.
[24] Y.C. Wang, T.M. Chou, M. Libera, E. Voelkl, B.G. Frost, Measurement of Polystyrene Mean Inner Potential by Transmission Electron Holography of Latex Spheres, Microsc. Microanal. 4 (1998) 146–157.
[25] M. Van Heel, M. Schatz, Fourier shell correlation threshold criteria, J. Struct. Biol. 151 (2005) 250–262.
[26] P.A. Penczek, Methods in Enzymology Vol. 482 (2010) 73–100.
[27] M. Guizar-Sicairos, et al., Role of the illumination spatial-frequency spectrum for ptychography, Phys. rev. B 86 (2012), 100103.
[28] A. Eljarrat, J. Müller, M.R.S. Huang, C.T Koch, Multi-focus TIE algorithm including partial spatial coherence and overlapping filters, Opt Express 26 (2018) 11819–11833.
[29] A. Parvizi, W.V.d. Broek, C.T. Koch, Recovering low spatial frequencies in wavefront sensing based on intensity measurements, ADV. STRUCT. CHEM. IMAGING 2 (2016) 3.
[30] R. Vincent, Phase retrieval in TEM using Fresnel images, Ultramicroscopy 90 (2002) 135–151.
[31] Y. Takahashi, et al., Automated acquisition of vast numbers of electron holograms with atomic-scale phase information, Microscopy 69 (2020) 132–139.
[32] I. Zanette, et al., Phase-Vortex Removal for Quantitative X-Ray Nanotomography with Near-Field Ptychography, Phys Rev Appl 14 (2020), 064078.
[33] J. Verbeeck, et al., Demonstration of a 2 × 2 programmable phase plate for electrons, Ultramicroscopy 190 (2018) 58–65.
[34] A.H. Tavabi, et al., Generation of electron vortices using nonexact electric fields, Phys. Rev. Research 2 (2020), 013185.